Journal of Nuclear Materials 406 (2010) 73–83

Contents lists available at ScienceDirect

Journal of Nuclear Materials

journal homepage: www.elsevier.com/locate/jnucmat

Characterization of neutron-irradiated ferritic model alloys and a RPV steel from combined APT, SANS, TEM and PAS analyses

E. Meslin [a,b,*], M. Lambrecht [c], M. Hernández-Mayoral [d], F. Bergner [e], L. Malerba [c], P. Pareige [b], B. Radiguet [b], A. Barbu [a], D. Gómez-Briceño [d], A. Ulbricht [e], A. Almazouzi [c,1]

[a] Service de Recherches de Métallurgie Physique, CEA/Saclay, 91191 Gif-sur-Yvette Cedex, France
[b] Groupe de Physique des Matériaux UMR-CNRS 6634, Equipe de Recherche Technologique, No. 1000, Université de Rouen, B.P. 12, 76801 Saint Etienne du Rouvray, France
[c] Nuclear Materials Science Institute, SCK-CEN, B-2400 Mol, Belgium
[d] CIEMAT, Division of Structural Materials, Avenida Complutense, 22, 28040 Madrid, Spain
[e] Forschungszentrum Dresden-Rossendorf, Institute of Safety Research, P.O. Box 510119, 01314 Dresden, Germany

ARTICLE INFO

Keywords:
RPV steels
Microstructure
Neutron irradiation
Radiation damage
APT
TEM
PAS
SANS

ABSTRACT

Understanding the behavior of reactor pressure vessel (RPV) steels under irradiation is a mandatory task that has to be elucidated in order to be able to operate safely a nuclear power plant or to extend its lifetime. To build up predictive tools, a substantial experimental data base is needed at the nanometre scale to extract quantitative information on neutron-irradiated materials and to validate the theoretical models. To reach this experimental goal, ferritic model alloys and French RPV steel were neutron irradiated in a test reactor at an irradiation flux of 9×10^{17} nm^{-2} s, doses from 0.18 to 1.3×10^{24} nm^{-2} and 300 °C. The main goal of this paper is to report the characterization of the radiation-induced microstructural change in the materials by using the state-of-the-art of characterization techniques available in Europe at the nanometre scale. Possibilities, limitations and complementarities of the techniques to each other are highlighted.

1. Introduction

The application of experimental techniques to the microstructural characterization of neutron-irradiated ferritic model alloys of increasing complexity has contributed to the mechanistic understanding of irradiation embrittlement of reactor pressure vessel (RPV) steels [1]. Simultaneously, modeling in this field has been characterized by the evolution from empirical models of prediction of the ductile to brittle transition temperature (DBTT) shift [2], via mechanistically-based correlations (MBC) [3,4] to multi-scale multi-physics (MSMP) models [5,6]. The latter aim at being sufficiently reliable to be safely extrapolated to never tested conditions, especially high doses. The availability of models of this type will also help reducing the amount of experiments needed, thereby reducing the need to produce, handle, test and store radioactive materials. To be applied to irradiation embrittlement, dedicated experiments on ferritic model alloys are required to identify the basic mechanisms responsible for embrittlement and to constitute a thorough experimental validation of the submodels at the appropriate time and space scale. These models are supposed to be developed fully based on physical considerations, without fitting. The validation provides thus an indication of whether all relevant mechanisms have been understood and introduced or not. In this context, the European PERFECT project was initiated [7] to bring together the knowledge gained in Europe and abroad from the various disciplinary involved in the phenomena of radiation effects on the mechanical performance of reactor pressure vessel steels. The approach adopted was to investigate Fe-base materials of increasing complexity irradiated in a test reactor. The main goal of this paper is to report on the nanometer-scale characterization of these materials.

Among the experimental techniques able to detect the irradiation-induced microstructural changes at this scale, atom probe tomography (APT), small-angle neutron scattering (SANS), transmission electron microscopy (TEM) and positron annihilation spectroscopy (PAS), play a particular role. It turned out that, because of the complexity of the problem as well as particular strengths and weaknesses of the individual techniques, there is no single method capable of solving all the related issues. Therefore, combinations of two or more techniques were applied to the materials in order to get a more complete picture including composition, morphology

* Corresponding author at: Service de Recherches de Métallurgie Physique, CEA/Saclay, 91191 Gif-sur-Yvette Cedex, France. Tel.: +33 1 69082168; fax: +33 1 69086667.
E-mail address: estelle.meslin@cea.fr (E. Meslin).
[1] Present address: EDF R&D renardières, 77250 Ecuelles, France.

0022-3115/$ - see front matter © 2010 Elsevier B.V. All rights reserved.
doi:10.1016/j.jnucmat.2009.12.021

and distribution of the irradiation-induced features [8–13]. Few investigations in the literature make use of a synergistic combination of the results obtained from different methods (e.g. [9]). The aim is to demonstrate the complementarity of different techniques as well as synergisms while focusing on combinations between APT, SANS, TEM and PAS.

These methods as well as the compositions and the irradiation conditions of materials [14] are briefly introduced in Section 2. Section 3 is devoted to the results obtained by each individual technique (APT, SANS, TEM and PAS). They are individually described in Refs. [15–18]. The whole set of results is exploited in Section 4 in order to obtain a coherent picture of irradiation damage in the present case and of the effects of dose and of the alloying elements, mainly Cu, Mn and Ni.

2. Experimental details

2.1. Materials and irradiation conditions

Fe-base alloys with increasing complexity were studied: Pure iron, low copper Fe–0.1 Cu (wt.%), high copper Fe–0.3 Cu, copper-free Fe-1.2 Mn–0.7 Ni, Fe–0.1 Cu–1.2 Mn–0.7 Ni and a 16MND5 RPV steel. The materials were prepared using argon-arc melting and zone refinement methods, starting from electrolytic iron. The resulting ingots were cold-worked after austenization tempering. A final heat treatment at 1075 K for 1 h was performed to release the stresses and to get well-recrystallized materials. The resulted model alloys were essentially composed of ferrite grains having a size ranging from 50 to 200 μm when going from the quaternary alloy (FeCuMnNi) to pure Fe. The average initial dislocation density was very similar in all alloys of about 5×10^{13} m^{-2}.

The nominal compositions of the fabricated materials were controlled by chemical analysis (CA). The results are given in Table 1. They were performed at EDF R&D (France) by ICP/MS (Induced Coupled Plasma/Mass Spectrum), except for the free carbon within the matrix, measured by internal friction at SCK-CEN (Belgium). The compositions were checked by APT analysis at the University of Rouen (France) before irradiation in the Fe–0.1Cu, FeMnNi, FeCuMnNi model alloys and in the RPV steel. CA and APT measurements performed in the Fe–0.1Cu and FeMnNi alloys are in good agreement. In the FeCuMnNi alloy, the APT measurements gave lower values than CA. The difference is most probably due to the non-homogeneous distribution of the alloying elements in the whole produced ingots. While in the case of the RPV steel, the observed depletion in Mn and C is certainly due to the presence of carbides, observed by TEM. Furthermore, the APT analyses were used to check the initial distribution of the solutes known to precipitate under irradiation (Cu, Mn, Ni and Si). The statistical χ^2 test confirmed their homogeneous distribution at the nanometer scale before irradiation.

The neutron irradiation was conducted at 300 °C and 150 bars in the CALLISTO loop of the BR2 test reactor at SCK-CEN (Mol, Belgium) to mimic the temperature and pressure of RPV steels in PWR reactors. The materials were wrapped tightly in steel capsules to avoid their contact with the cooling water and to ensure a high thermal conductivity in the whole capsule. The average temperature measured by the numerous thermometers (more than 14 per capsule) was (300 ± 5) °C. The specimens were exposed to a constant neutron flux of 9×10^{17} nm^{-2} s^{-1} ($E > 1$ MeV). The reached neutron doses were determined via the analysis of the multiple flux monitors that were inserted in each capsule. Four irradiation campaigns have been performed to accumulate increasing doses ranging from 0.18 to 1.3×10^{24} nm^{-2} ($E > 1$ MeV). In terms of displacement per atom (dpa) and by using the widely accepted cross-section of 1500 barns for neutrons of energy higher than 1 MeV, these conditions correspond to a dose rate of about 1.4×10^{-7} dpa s^{-1} and to four doses (0.025, 0.05, 0.1 and 0.2 dpa). It is worth mentioning that 0.1 dpa corresponds to about 40 years of operation of pressurized water reactors. A more detailed description of the materials including exact material compositions, irradiation conditions and mechanical characterization before irradiation can be found in Ref. [14].

The investigation by means of the four microstructural characterization methods involved was not conducted for the whole set of materials. For the sake of clarity, the conditions studied by every characterization technique are gathered in Table 2.

2.2. Atom probe tomography (APT)

The kinetic of solute clustering after irradiation was followed by APT [19]. This technique is known to be a very efficient tool for the chemical analyses of solute-enriched clusters. Their characteristics – number density, size and composition – as well as the matrix composition are accurately determined in the volume accessible. Analyses were performed at set-up developed at the University of Rouen (France). To reduce the energy spread of emitted ions, they were conducted with an energy compensating device (a reflectron lens). Furthermore, to avoid the preferential evaporation of copper, the experiments were carried out at a cryogenic temperature of 50 K and with an electrical pulse fraction of 20% of the standing voltage. All the experiments were performed with a pulse rate limited to 0.03 atom/pulse to reduce the risk of failure of the needle-shape sample. The analyzed volume was typically $15 \times 15 \times 100$ nm^3 for each sample. More details about the treatment of the data and how to get the essential information out of them can be found in Ref. [15].

Table 1
Nominal compositions of the ferritic alloys and of the RPV steel obtained by chemical analyses (CA) and AP measurements. AP measurements in the 16MND5 RPV steel revealed also the presence of Mo, Al, Cr and Co with a respective content of 0.39 ± 0.04, 0.02 ± 0.01, 0.24 ± 0.01 and 0.03 ± 0.01 at.% in agreement with the literature [55–57].

Material	at.%	Cu	Mn	Ni	C	P	Si
Pure iron	CA	<0.004	0.007	<0.005	<0.01	0.01	0.009
Fe–0.1Cu	CA	0.079	0.010	<0.005	<0.01	0.011	0.01
	AP	0.085 ± 0.006	–	–	–	0.0045 ± 0.001	–
Fe–0.3Cu	CA	0.28	0.006	<0.005	<0.01	0.014	<0.009
FeMnNi	CA	<0.005	1.11	0.71	<0.01	0.009	<0.01
	AP	–	1.12 ± 0.02	0.73 ± 0.01	–	0.0045 ± 0.001	–
FeCuMnNi	CA	0.092	1.11	0.68	<0.01	0.009	<0.01
	AP	0.068 ± 0.006	0.98 ± 0.02	0.57 ± 0.02	–	0.0034 ± 0.0015	–
16MND5	CA	0.056	1.31	0.71	0.65	0.013	0.385
	AP	0.05 ± 0.01	1.07 ± 0.06	0.6 ± 0.05	0.048 ± 0.01	0.008 ± 0.006	0.48 ± 0.04

Table 2
Overview of the methods applied to the individual materials.

Material	Neutron dose (dpa)	Methods applied			
Pure Fe	0.025			PAS	TEM
	0.05				TEM
	0.1			PAS	TEM
	0.2	SANS		PAS	TEM
Fe–0.1Cu	0.025	SANS	APT	PAS	TEM
	0.05	SANS	APT	PAS	TEM
	0.1	SANS	APT	PAS	TEM
	0.2	SANS	APT	PAS	TEM
Fe–0.3Cu	0.025	SANS		PAS	TEM
	0.05	SANS		PAS	TEM
	0.1	SANS		PAS	TEM
	0.2	SANS		PAS	TEM
FeMnNi	0.025		APT	PAS	
	0.05	SANS	APT	PAS	
	0.1	SANS	APT	PAS	TEM
	0.2	SANS	APT	PAS	TEM
FeCuMnNi	0.025		APT	PAS	
	0.05	SANS	APT	PAS	
	0.1	SANS	APT	PAS	TEM
	0.2	SANS		PAS	
RPV steel	0.025			PAS	TEM
	0.05	SANS		PAS	TEM
	0.1	SANS		PAS	TEM
	0.2	SANS	APT	PAS	TEM

2.3. Small-angle neutron scattering (SANS)

Small-angle neutron scattering (SANS) is capable of characterizing the size distribution of nm-sized irradiation-induced defect-solute clusters in ferritic alloys. This is done by measuring the scattering cross-section in a saturation magnetic field applied to the sample, separating nuclear and magnetic contributions from the anisotropy introduced by the magnetic field, subtracting the scattering cross-section for an unirradiated control sample and calculating the size distribution by solving an inverse problem. The lower detection limit is about 0.5 nm in cluster radius. An advantage is the averaging capability resulting from a probed volume of some 10 mm^3 and from a number of scattering events of the order of 10^6. In addition, some integrated information on the average cluster composition is given by the ratio of magnetic and nuclear scattering as described in Section 4.2.

The experiments were performed at the SANS facilities at PSI Villigen [20] (Switzerland) and LLB Saclay [21] (France) by SCK-CEN (Belgium) and the data analysis was performed by FZD (Germany). The measuring procedure and analysis are described in detail in Ref. [16]. We assumed a dilute two-phase matrix-inclusion microstructure composed of non-magnetic spherical scatterers randomly dispersed in a pure Fe matrix. The indirect transformation method [22] was applied in order to derive the size distribution of scatterers without assuming a certain type of distribution.

2.4. Transmission electron microscopy (TEM)

Microstructure of neutron-irradiated materials was examined by TEM with a microscope JEOL type, model JEM-2010 operating at 200 keV, at CIEMAT (Spain). This technique is able to detect clusters of point defects (vacancies or interstitials) induced by irradiation, with sizes over 1.5 nm. It is worth to point out that information from the interstitial component of the radiation damage can be obtained. It is not detected with other microstructural characterization techniques in such a direct way.

Diffraction contrast methods were employed for imaging defect microstructure according to methodologies described, for instance, in Refs. [23,24]. From TEM images, quantitative information was obtained about the density and size of the observed defects. Counting of defects was performed on TEM images recorded under reflections type $g = (1, 1, 0)$ where the best contrast was obtained. The presence of voids was studied by means of a through-focal series recorded with the foil tilted away from the Bragg condition for all reflections [23,24]. The trend of microstructure evolution has been studied in terms of defect density and defect size. A full description of the methodology employed is described in Ref. [17].

2.5. Positron annihilation spectroscopy (PAS)

It is known that positrons are very sensitive to all types of vacancy–clusters and vacancy–solute complexes [13]. As these defects will play an important role in the formation of the features causing hardening, positron annihilation spectroscopy (PAS) is an excellent technique to investigate their behavior under irradiation, in order to obtain a complete understanding of the irradiation-induced damage. Indeed, in this technique, the positron is applied as a probe. As antiparticle of the electron, the positron is trapped by defects with a different electron density than the bulk material, such as vacancies, vacancy clusters, interfaces, second phase particles, dislocations, etc. [25]. Moreover, due to the difference in positron affinity of the different atomic species, positrons annihilate with a different probability in the precipitates as compared to the bulk material [26]. The power of PAS lies in its possibility to find very small defects (>0.1 nm) even in very low concentrations (>1 ppm), its "self-seeking" nature and its non-destructiveness.

Positron lifetime measurements were also performed at SCK-CEN, using the same procedure as described by Jardin et al. [27]. These measurements provide information on the size and density of small vacancy-type defects. This information is not easily withdrawn. Vehanen et al. [28] proposed a mechanism to analyze the positron experiments and to calculate the size and density, starting from the positron lifetime results. The positron trapping model in the presence of two types of defects was lately used to estimate size and density of the defects [29].

3. Results

3.1. APT

Solute-enriched clusters were detected after irradiation in the four materials studied by APT (Fig. 1), but were found to be very diffuse. The proportion of iron within the clusters is always higher than 50%. There is a controversy about the iron content in radiation-induced clusters reported by atom probe analyses in low copper ferritic materials ([Cu] < 0.1 wt.%). Indeed, some authors found very diffuse clusters [30–34], in agreement with our measurements, while others reported clusters with a very low amount of iron [35–37]. This discrepancy is certainly due to the difference in the algorithm used to characterize clusters. A description of the maximum separation envelope method referring to Refs. [35–37] can be found in Ref. [38] while the description of the method used in this study can be found in Ref. [15].

Phosphorous atoms gather also, in association or not with other solutes, even though the amount of phosphorous is expected to be quite low in these model alloys. The whole set of results obtained is given in Table 3 and Figs. 2–5. The precipitated volume fraction was calculated taking into account the proportion of solute atoms (iron excluded) within clusters (Fig. 2) [39], to be in consistency with the hypothesis of non-magnetic scatterers assumed to interpret the SANS data. Volume fractions obtained with iron included are also given for comparison.

In the low copper Fe–0.1Cu alloy, copper-enriched clusters were formed after irradiation starting from the lowest dose of 0.025 dpa.

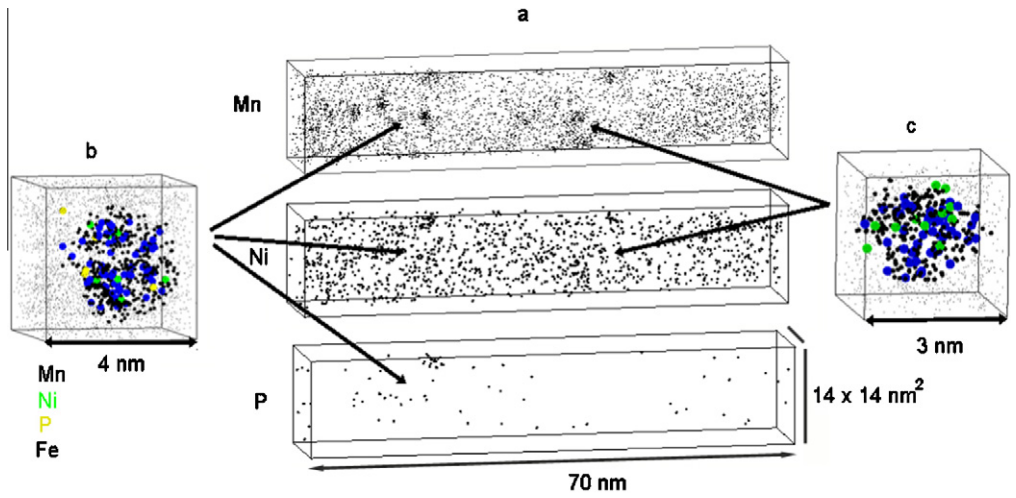

Fig. 1. (a) APT reconstitution of a small volume of the FeMnNi alloy after neutron irradiation up to 0.2 dpa. Iron atoms are not represented for clarity of the image. (b and c) Enlargement of manganese and nickel enriched clusters.

Table 3
Summary of the APT results. *N* is the number of clusters detected in each case.

Material	Irradiation dose (dpa)	*N*	Cluster composition (at.%)			
			Group[a]	Cu	Mn	Ni
Fe–0.1Cu	0.025	4		–[b]	–	–
	0.05	3		23 ± 5	–	–
	0.1	3		11.5 ± 2	–	–
	0.2	6		25 ± 6	–	–
FeMnNi	0.1	11		–	9.1 ± 0.7	3.3 ± 0.5
	0.2	14		–	13.7 ± 2	3.4 ± 1
FeCuMnNi	0.025	3	1	8.9 ± 0.3	3.9 ± 0.1	1.6 ± 0.1
	0.05	9	1	8.3 ± 2.1	3 ± 1.8	2.4 ± 1.1
	0.1	3	1	13.3 ± 2.3	3.5 ± 3.5	4.7 ± 2.8
		13	2	0.7 ± 0.7	6.4 ± 3.3	4.4 ± 4.4
RPV steel	0.2	16		–	8.4 ± 1.7	–

[a] Two cluster groups were detected. Clusters of group 1 are mainly enriched in copper while clusters of group 2 are only enriched in manganese and nickel.
[b] All the clusters were located at the edge of the analyze cylinder. Thus, the composition of clusters cannot be determined.

Their number density is equal to 10^{23} m^{-3} and stayed constant up to 0.2 dpa, the highest dose reached (Fig. 3), in agreement with previous results obtained by APT or SANS in binary Fe–Cu alloys [33,10]. The cluster nucleation was thus already finished at 0.025 dpa and no coarsening occurred. In addition, from 0.025 to 0.2 dpa, the precipitated volume fraction (iron excluded) increases from (0.019 ± 0.003)% to (0.064 ± 0.004)%, indicating a cluster growth with dose.

In the copper-free FeMnNi alloy, no cluster was detected after irradiation at the two lowest doses reached: 0.025 and 0.05 dpa, but the distribution of manganese was not homogeneous in both cases and the distribution of nickel was not homogeneous after irradiation at 0.05 dpa. After a dose of 0.1 dpa, clusters enriched in manganese and nickel or in manganese only were formed. Their number density stayed unchanged up to 0.2 dpa (Fig. 3), while the solute precipitated volume fraction increased (Fig. 2), so the cluster grew during irradiation with dose.

In the FeCuMnNi alloy, two clusters groups could be distinguished (Table 3). Clusters of group 1 were formed from the lowest dose of 0.025 dpa. They are mainly enriched in copper. Their enrichment in solute was quantified by applying the relation (2) in Ref. [15]. We found a copper enrichment greater than 100 whereas the manganese and nickel enrichments are limited to few units (2–8). Clusters of group 2 appeared only after a dose of 0.1 dpa, therefore much later than clusters of group 1. They are enriched in manganese and nickel or in manganese only. The mean enrichments in manganese and nickel are equal to 6 and 7, respectively.

Results obtained in the Fe–0.1Cu, FeMnNi and FeCuMnNi model alloys indicated that copper clusters formed earlier than manganese and nickel ones. The first were detected at the lowest dose of 0.025 dpa while the second formed after a higher dose of 0.1 dpa. This experimental finding could most probably be attributed to the difference in the solute clustering process. Indeed under irradiation, two mechanisms may explain the solute clustering. The first one is an irradiation-enhancement of the diffusion, due to the supersaturation of mobile vacancies at the irradiation temperature. The second one is a more complex mechanism of irradiation-induced clustering, generated by the flux coupling between mobile point defects and solute. The former is mediated by the same driving force than the one operating during the copper clustering under the thermal ageing of Cu-rich steel or Fe-alloys. It can thus only occur in a supersaturated solid solution. Since copper is highly insoluble in the α-iron at 300 °C, while manganese and nickel are soluble, at least in their respective binary system, manganese and nickel segregation may just be induced by the irradiation, while copper clustering may also result of an irradiation-enhancement. In addition, the comparison between results obtained in the Fe–0.1Cu and FeCuMnNi alloys shows that the copper precipitation kinetic is decreased in the presence of manganese and nickel. It is in consistency with findings from a rate theory model calibrated from the TEM distributions of point defect clusters formed during irradiation in the same model alloys. Indeed, it reveals that the experimental results could be reproduced by increasing the migration energy of vacancies in the more complex alloy [40,41]. Since it is well known that the transport of copper occurs mainly via vacancies (e.g. [6]), our experimental APT observation can be explained by the reduction of the vacancy mobility in presence of manganese and nickel, which may delay the copper precipitation.

The 16MND5 RPV steel was investigated by APT after irradiation up to 0.2 dpa. The clusters detected were found to be enriched in manganese only.

3.2. SANS

For a complete description of the obtained scattering curves and size distributions we refer to Ref. [16], here the emphasis is put on

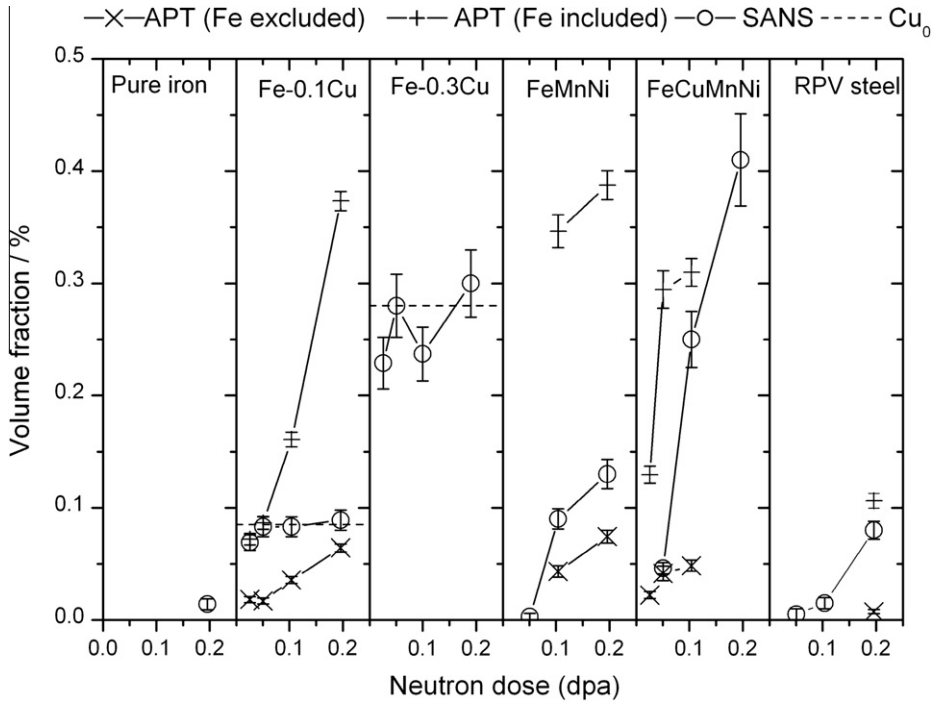

Fig. 2. Total volume fraction of radiation-induced damage as functions of dose obtained from SANS and APT measurements. SANS results were obtained by assuming non-magnetic scatterers. The volume fractions, Cu_0, corresponding to the Cu content of the Fe–0.1Cu and Fe–0.3Cu alloys are indicated by dashed lines. Precipitated volume fractions detected by APT were calculated with and without iron included. Since solute-enriched clusters contained a large amount of iron and/or are associated with vacancies, we assumed that all the solute atomic volumes were equal to the iron atomic volume for these calculations (solute relaxation).

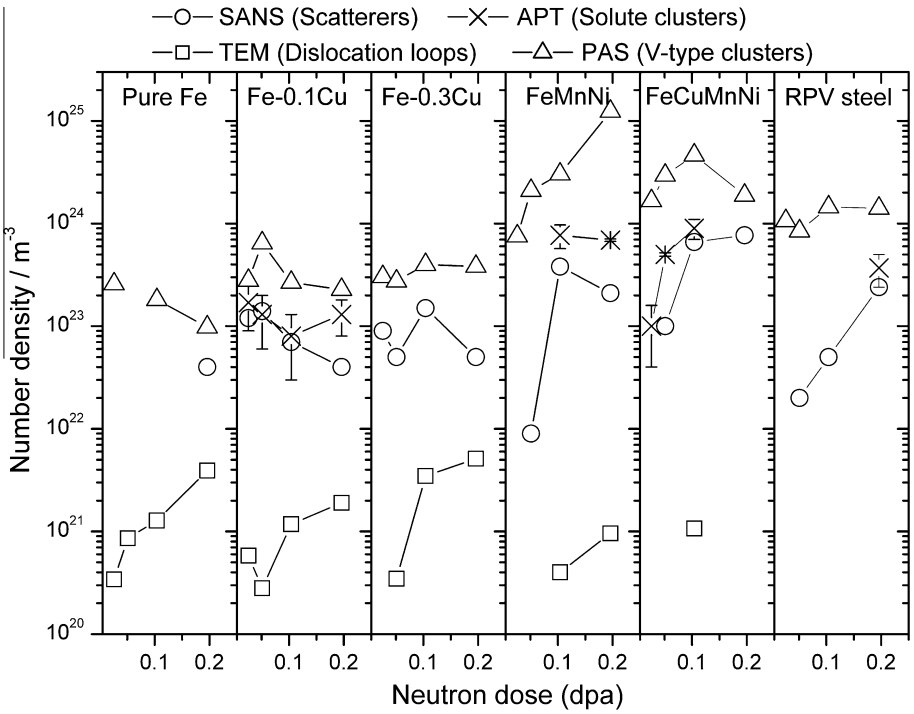

Fig. 3. Number density of radiation-induced damage as functions of dose from APT, SANS, TEM and PAS measurements.

the data interpretation. The size distributions obtained are essentially single-peaked. The total volume fraction of clusters, the estimated number density (integrated from the lower detection limit, 0.5 nm, upwards), the radius at the peak of the size distribution and the *A*-ratio, found for each investigated alloy and condition according to Ref. [42], are summarized in Figs. 2–5. Here, $A = 1 + M/N$, where M and N denote the magnetic and nuclear contributions to the total intensity integrated in the size space. It is important to remind that the size distributions were obtained based on the assumption of a dilute two-phase matrix-inclusion microstructure composed of non-magnetic spherical scatterers randomly dispersed in a pure Fe matrix.

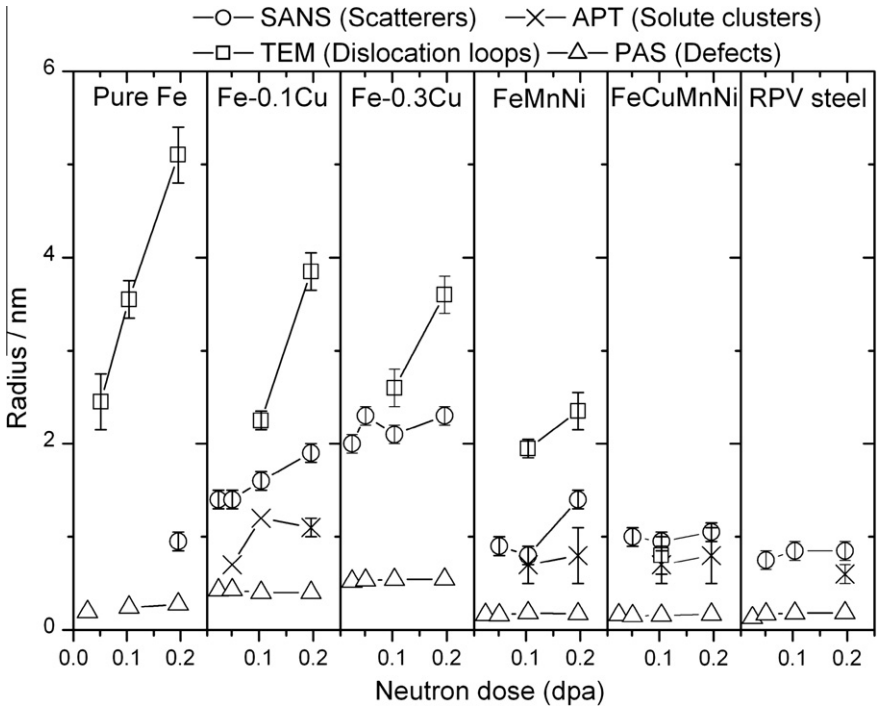

Fig. 4. Evolution of the radius of radiation-induced damage from APT, SANS, TEM and PAS measurements during neutron irradiation. The peak radius of the size distribution of scatterers in terms of volume fraction is indicated for SANS. The mean radius of the size distribution in terms of number density is given for both TEM and APT. In the latter case, some of the results have no error bars because they correspond to one cluster only. Others clusters detected were located at the edge of the analyze cylinder. For PAS, the mean size of (Cu–V) clusters in Fe–Cu binary alloys and V-clusters in all other alloys is given (see text for more explanation).

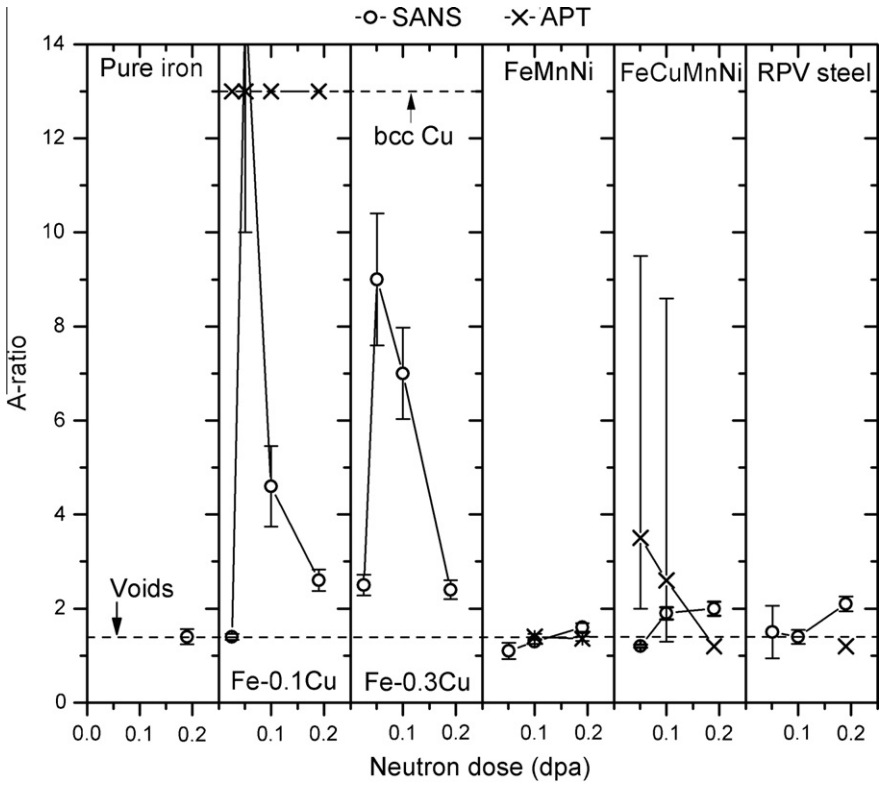

Fig. 5. Magnetic to nuclear scattering ratios (*A*-ratio) measured by means of SANS as functions of dose. Theoretical *A*-ratios for pure nanovoids and pure, fully coherent bcc Cu clusters are indicated. Mean values and upper and lower bounds of the *A*-ratio were also calculated from the cluster compositions deduced from APT (Table 3) using Eq. (1).

It is observed (Fig. 2) that the binary Fe–Cu alloys exhibit a saturation-like behavior of the volume fraction. The saturation value corresponds to about the atomic fraction of Cu in both alloys, namely 0.085 and 0.28 at.%, indicated by dashed lines in the figure.

It is important to note that this does not mean that all Cu is in the clusters. In fact, clusters may also contain Fe atoms (as indicated by APT) and vacancies (as indicated by PAS). As for the other materials, a monotonous increase of the volume fraction as a function of dose is observed in the covered dose range. In the Ni- and Mn-containing alloys the dose range of the steepest increase is delayed in comparison with pure Fe and binary Fe–Cu alloys. The sum of the volume fractions for the Fe–0.1Cu and FeMnNi alloys is smaller than the volume fraction observed for the FeCuMnNi alloy (for instance at 0.2 dpa: 0.089 vol.% (in Fe–0.1Cu) + 0.13 vol.% (in FeMnNi) < 0.41 vol.% (in FeCuMnNi)), indicating a synergistic effect of Cu and Mn/Ni.

For pure Fe and the binary Fe–Cu alloys, an increase of cluster size as a function of both Cu-level and dose is observed (Fig. 4). For the other alloys the peak radius is about 1 nm for all investigated conditions and there is no clear dose dependence.

In the case of pure Fe the measured *A*-ratio agrees well with the value expected for any kind of self-defects, vacancy clusters in particular, $A = 1.4$, indicated in Fig. 5. For both binary Fe–Cu alloys, the *A*-ratio exhibits similar dose dependence and passes through a maximum at about 0.05 dpa. This dependence can be interpreted in terms of the Cu-fraction of mixed Cu-vacancy clusters also passing through a maximum located near 100% Cu at a dose of about 0.05 dpa. Smaller values of the *A*-ratio that are partly even falling below the value of self-defects are characteristic of the complex alloys. This is clear evidence for the dominant role of the Mn-content in the defect-solute clustering process. In fact, Mn is the only element presenting a negative nuclear scattering length and, therefore, being capable of reducing the *A*-ratio to a value below 1.4. There seems to be a tendency of the *A*-ratio to increase with dose for the complex alloys.

3.3. TEM

Fig. 6 shows, as an example, a TEM image of the microstructure produced in pure Fe by neutron irradiation up to 0.2 dpa. Damage observed from 0.025 to 0.2 dpa by diffraction contrast methods was in the form of directly observable defects identified as small dislocation loops. These defects were distributed homogeneously in the matrix, though in some cases dislocation decoration was also observed. Visible loops increased in size with dose but no overlap was observed in this dose range.

It has been found that in pure Fe irradiated to 0.2 dpa, the majority of dislocation loops have a ⟨1 0 0⟩ Burgers vector type, and they are believed to be of interstitial nature in agreement with results in literature for similar experimental conditions [40,43,44]. However, the fact that some of the smaller dislocation loops are vacancy in nature is not discarded, though it is not probable that large dislocation loops are vacancy type as pure vacancy clusters are more stable, in general, spherical in shape. The presence of voids was studied in the case of pure Fe neutron irradiated up to 0.2 dpa, where large voids with average size of (12 ± 0.4) nm and estimated density of $1.2 \times 10^{20}\ m^{-3}$, were observed. In addition, small voids were found, with sizes of about 2 nm, were also detected. Large and small voids appear to be randomly distributed throughout the grain interior, the large ones appeared some times associated to dislocation lines, but they were not observed to appear preferentially associated to dislocation loops.

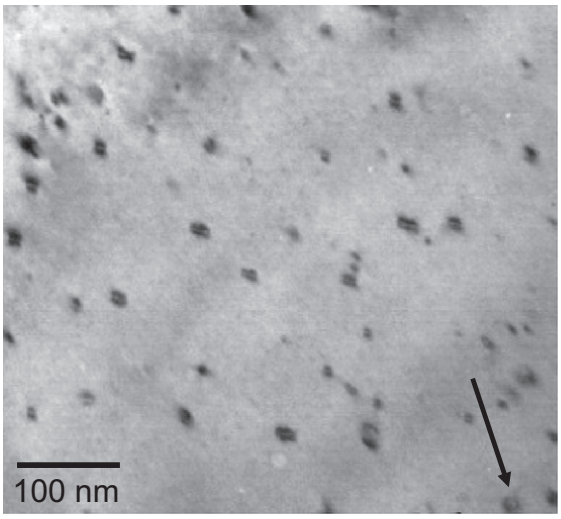

Fig. 6. TEM image of a neutron-induced microstructure in pure Fe at 0.2 dpa.

In the rest of the model alloys, a similar neutron-induced microstructure was found, regarding the presence of defects in the form of dislocation loops. TEM examinations in order to study the possible presence of a population of voids are still underway. On the other hand, the RPV steel was also examined before and after neutron irradiation, and no defects that could be attributed to neutron exposure were observed.

Quantitative information that was obtained from TEM images regarding density and size distribution of defects of interstitial type is summarized in Figs. 3 and 4. Also, Fig. 7 shows defect size distributions in the form of histograms for different doses and model alloys. It is worth noting that defect size on histograms refers to the larger dimension, i.e. diameter, of the observed defects.

Defect density increases for the case of pure Fe when dose increases from 0.025 to 0.2 dpa; the data are consistent with a linear dependence. In both Fe–Cu alloys the observed effect of dose was similar to what was found in pure Fe, namely, dislocation loop density increases with increasing dose, though a linear dependence cannot be stated as in pure Fe. A clear effect of copper content on defect density could not be extracted. However, the presence of Cu influences the proportion of types of Burgers vector of the observed clusters. In fact, the percentage of ½ ⟨1 1 1⟩ increased from 14% in pure Fe to 37% in the Fe–0.3Cu alloy, at 0.2 dpa.

Regarding the effect of dose, a clear influence on size distribution is observed. The histograms illustrating the size distribution become broader as the dose increases in all the model alloys, meaning that interstitial clusters grow as dose accumulates from 0.025 dpa upwards. Thus, maximum size increases with dose and the same happens to mean size. The growth of existing clusters occurs together with the generation of new ones as a population of defects with size at the resolution limit of TEM, 1.5–2 nm, is always observed.

Also a clear effect of composition on size distribution is observed. This becomes narrower in both Fe–Cu alloys compared to pure iron. Indeed, the average cluster size decreases with respect to pure Fe for the same irradiation dose and maximum cluster sizes reached by the interstitial loops are also smaller than in pure Fe. This means that the presence of copper in the material reduces the rate of growth of interstitial clusters being necessary a higher dose to reach a similar size as in pure iron.

As for the other alloys, the effect of composition on size distribution is more pronounced in the case of the FeCuMnNi and FeMnNi alloys where the lowest average sizes and the narrowest size distributions are obtained. It is observed in fact that average size decreases as the system becomes more complex, as it was also observed in ferritic model alloys under cascade damage ion irradiation [41].

The FeMnNi copper-free alloy showed the lowest density among all the investigated alloys. Size distribution is also narrower than in pure Fe and the Fe–Cu alloys, similar to the FeCuMnNi alloy. This indicates that both, Mn and Ni atoms, hinder the interstitial loop growth and over more they seem to suppress the

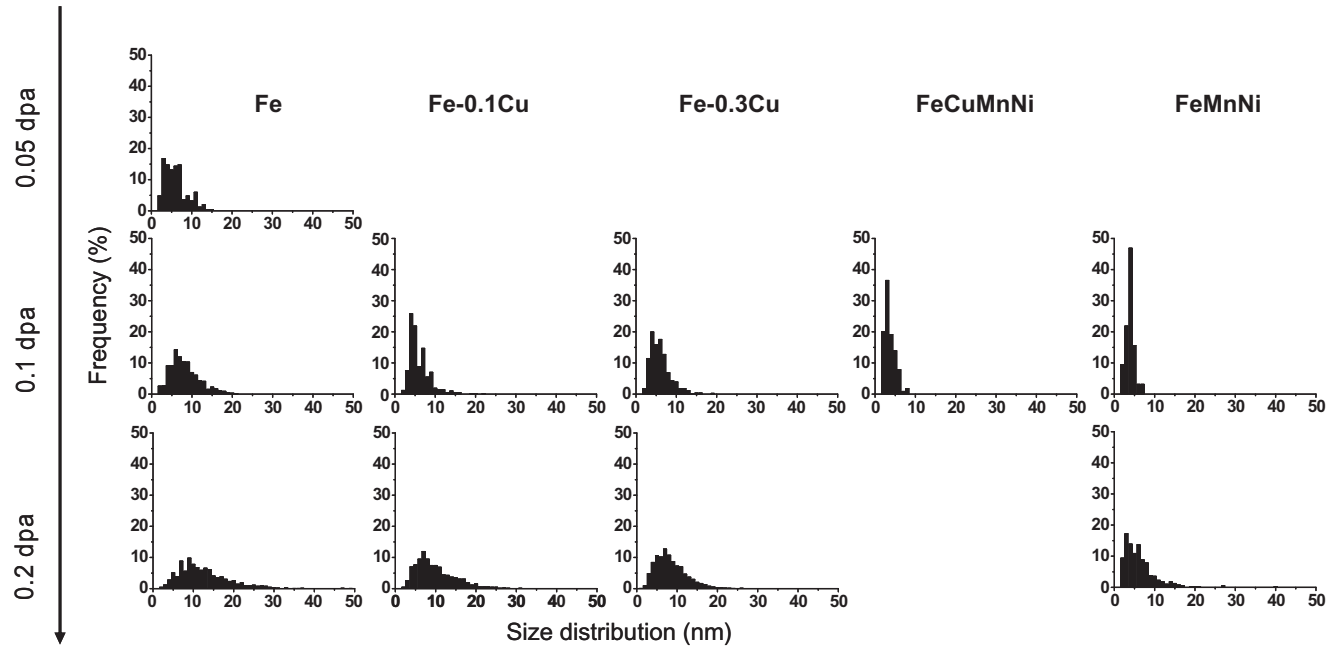

Fig. 7. Size distributions of neutron-induced dislocation loops in model alloys showing dose and composition influence. Size is given in terms of diameter.

dislocation loop development, as a fairly reduced number density of the dislocation loops compared to that for iron was observed. Hence, TEM results reflect a possible interaction of Mn and Ni atoms with interstitial point defects or clusters.

Results from TEM regarding interstitial component of damage in the form of dislocation loops, show that the kinetics of formation and growth of this type of defects are influenced by the alloying elements present in the material.

3.4. PAS

The size and the density of the defects detected by PAS have been calculated using the approach described in Ref. [29]. The resulting average values are depicted in Figs. 3 and 4. Care should be taken about the fact that the size is calculated depending on the average amount of vacancies present in the clusters. As it is known that the vacancy clusters, which are produced during irradiation, are mostly decorated with alloying elements, this method will underestimate the real size. On top of this, it is known that the copper plays an important role on the positron trapping behavior. It is therefore necessary to estimate the average copper coverage of the clusters. This has been done using the high momentum part of the coincidence Doppler broadening spectra. Using this average coverage, a better estimation of the amount of vacancies in the clusters could be performed. This leads to a much higher size in the binary Fe–Cu alloys, compared to the other model alloys.

It is assumed that the ternary alloys and those with higher compositional complexity will contain also vacancy clusters combined with alloying elements. But, it is not possible to separate the effects of the individual element. Therefore, the size obtained with positrons will be underestimated.

For the effective calculation of the density of the defects, a second short positron lifetime trap was included. These traps were assumed to be mono-vacancies combined with a foreign element. These features will play an important role in the formation of other defects, but it will not change their behavior.

For pure iron, it is observed that the size of the clusters increases gradually with the irradiation dose, while the number density of the clusters decreases. The clusters thus grow by agglomeration of smaller clusters. Newly produced vacancies (caused by the irradiation) will be distributed between the clusters and the bulk. The estimated diameter agrees with the one observed by Eldrup et al. (see Fig. 4 of [45]) for pure iron irradiated with neutrons in a test reactor at approximately the same dose at 70 °C. The number density of the defects, however, is about 10 times lower here than the one found by Eldrup et al., due most probably to the difference in irradiation temperatures. Indeed, at higher temperature, the vacancies, isolated or forming small clusters are more mobile and therefore a higher amount could be eliminated at sinks.

In the Fe–0.1Cu alloy, the vacancy clusters seem to be very stable with dose. Nevertheless, a small decrease of the vacancy clusters number density is found after about 0.05 dpa. This is most probably due to the agglomeration of the small clusters. Thereafter, the amount of clusters remains almost constant. Newly produced vacancies will thus be trapped by the clusters, as proposed by Verheyen et al. [46]. In the Fe–0.3 Cu, the cluster number density keeps on growing with irradiation dose. This indicates that there is still copper available in the matrix for forming new clusters. As more clusters can be formed in this alloy, the clusters will remain smaller in term of the included amount of vacancies. Nevertheless, the total vacancy-Cu clusters will be bigger due to a larger amount of copper atoms.

In the alloys containing manganese and nickel, the observed vacancy cluster sizes are extremely small, while the density of the defects is much higher compared to the other alloys. When also copper is available, the average density of the defects remains a little lower, compared to the alloy without copper. Therefore, it is believed that some clustering occurs, namely the formation of copper–vacancy complexes. Nevertheless, the amount of vacancies in these complexes remains very low. Also the results of the RPV steel indicate a great deal of very small vacancy clusters.

4. Discussion

4.1. TEM versus SANS

The scattering theory according to Seeger [47] has been applied in order to calculate the scattering cross-section expected from the

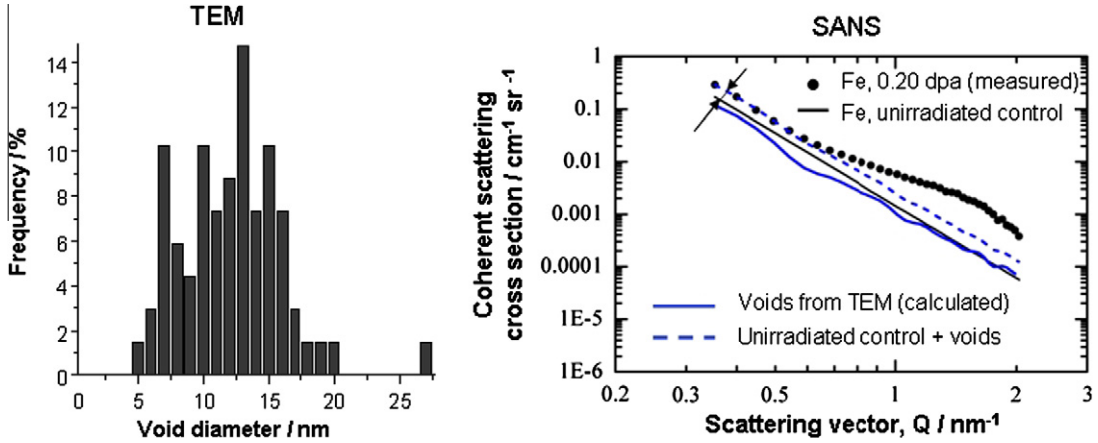

Fig. 8. Measured scattering cross-section for Fe, cross-section calculated on the basis of the size distribution of voids obtained by TEM for the same material and comparison of the resulting scattering cross-sections at low values of *Q*.

distribution of dislocation loops [48] detected by TEM for 0.2 dpa in pure Fe [17]. It turns out that the cross-section is orders of magnitude too small to explain the irradiation-induced increase of the scattering intensity in both the high-*Q* and low-*Q* range observed in Fig. 8 [48]. The same holds true, if the dislocation loops are interpreted as thin slices characterized by an average magnetic scattering length reduced with respect to the Fe matrix [49]. The conclusion that dislocation loops are not responsible for the observed increase of scattering cross-sections is also valid for the other materials and irradiation conditions considered. In this sense, TEM and SANS are complementary.

The scattering cross-section calculated from the distribution of nanovoids detected by means of TEM [17] for 0.2 dpa in pure Fe is shown in Fig. 8. We have found that this contribution is capable of explaining the irradiation-induced increase of the scattering cross-section observed at low values of the scattering vector, *Q*. The additional increase of cross-section at high *Q*-values, $Q > 1\ \mathrm{nm}^{-1}$, is interpreted as a second population of smaller vacancy clusters or depleted zones in pure Fe. The SANS data for pure Fe in Figs. 2–5 refer to the latter population only. Detectability of these clusters in the TEM is limited, but their detection has been successful in pure iron at 0.2 dpa in this work.

4.2. APT versus SANS

Information derived from APT and SANS analyses is partly overlapping. In fact, both methods give information on size, volume fraction and composition of clusters and can be cross-checked in these respects. Comparisons between results are given in Figs. 2–4. Clusters of size smaller than 0.5 nm were not detected by SANS. It results in a slight overestimation of cluster sizes by this method and an underestimation of their number density. However, uncertainties on the values of volume fraction are lower because small scatterers contribute little to volume fraction. Data obtained by APT are subjected to uncertainties also. Indeed, effects of local magnification and trajectory aberrations may slightly change the cluster radius obtained by APT, especially when they contain a non-negligible amount of vacancies. In the case of copper-rich clusters embedded in an iron matrix, it would result in an underestimation in the two directions perpendicular to the analyze direction. In addition, the cluster sizes are strongly correlated to the location of the cluster interface, which can be quite undefined, especially in the case of dilute clusters. To have a reproducible estimation, it is necessary to have a criterion. The criterion used in that study is described in Ref. [15]. In the case of the volume fraction (iron excluded), the estimation by APT may be slightly underestimated, if the solute clusters are associated with vacancies [50,51].

Concerning the cluster size, results are fully consistent with what was expected. APT measurements are slightly lower than SANS measurements (Fig. 4). In the case of the number density, results obtained in the Fe–0.1Cu alloy are in good agreement, probably because the proportion of small copper-enriched clusters is low. In the FeMnNi and the FeCuMnNi alloys and in the RPV steel, cluster number density obtained by SANS is lower than those detected by APT, as expected. Furthermore, the precipitated volume fractions obtained by SANS are slightly larger than those obtained by APT (iron excluded) (Fig. 2). The most prominent assumption for this difference is related to the magnetic character of the scatterers, i.e. the presence of iron within clusters. We reported in the same figure (Fig. 2), for comparison, the volume fractions deduced from APT results by including iron atoms detected within clusters. The values calculated are largely higher than those obtained by SANS. However, it is worth noticing that a fraction of 50% Fe in the clusters bearing the same magnetic moment as matrix Fe would result in a four times higher volume fraction, to compensate the reduced SANS contrast. It is important to note that despite of the uncertainty regarding the magnetic character of the scatterers, the volume fractions obtained by SANS on the assumption of non-magnetic scatterers are not meaningless. In fact, they still represent a lower bound of all possible volume fractions.

In order to confront results derived from APT and SANS in terms of cluster composition, it is worth estimating the A-ratio, according to Eq. (1) [52], using the cluster composition found by APT

$$A = 1 + \left(\frac{6.0(n_{\mathrm{Fe}} - 1) + 1.0 n_{\mathrm{Ni}}}{9.45(n_{\mathrm{Fe}} - 1) + 10.3 n_{\mathrm{Ni}} + 7.72 n_{\mathrm{Cu}} - 3.75 n_{\mathrm{Mn}}} \right)^2 \qquad (1)$$

The atomic fractions, n_X, were taken from Table 3. *A*-ratios corresponding to the average composition as well as lower and upper bounds were calculated (Fig. 5). It should be noticed that according to Eq. (1), the *A*-ratio of clusters composed of only one solute atom (e.g. mixed Cu–Fe) is independent of the Fe fraction in the clusters as long as the Fe atoms bear the same magnetic moment as matrix Fe. The *A*-ratio measured by SANS for Fe–0.1Cu (except for 0.05 dpa) is smaller than the values derived from the APT data. This may be due to two factors. First, the magnetic moment of Fe atoms in the cluster may be larger than those in the matrix [53]. Taking a 1.05 times higher moment [53], the *A*-ratio obtained from SANS may be reduced from a value of 13 to about 9. This effect is clearly not the dominant cause of the discrepancy, although it may contribute slightly. Second, the clusters may contain a vacancy

fraction, as observed by PAS, but not detected by APT causing the *A*-ratio to decrease up to a limit of 1.4 for pure vacancy clusters. The second argument sounds the most plausible at this stage.

For the FeMnNi and FeCuMnNi alloys and the RPV steel we partly observe deviations between average *A*-ratios obtained by SANS and *A*-ratios deduced from APT compositions. These deviations may be interpreted as being due to rather wide distributions of cluster composition. In fact, the average from a small ensemble of clusters as covered by APT may differ from the average observed for a macroscopic volume. Moreover, bimodal distributions of composition were directly observed by APT.

4.3. APT versus TEM

Information given by these two methods is distinct but complementary. Solute atoms clustering can be detected by APT while resolvable dislocation loops are visible by TEM. In the assumption of a heterogeneous precipitation of solute clusters on the point defect clusters [15,30,33], we expected the number density of the former to be at least equal to the number density of the latter. The apparent discrepancy shown in Fig. 4 is probably due to the detection limit of the TEM. Clusters of size lower than 1.5 nm in diameter are not taken into account. In addition, copper clusters segregated on a 10-nm size circular object were detected by APT in Fe–0.1Cu irradiated up to 0.2 dpa [41]. It corresponds probably to a 10-nm size decorated dislocation loop, which presence was confirmed by the TEM analysis.

4.4. PAS versus the other techniques

PAS is sensible to the vacancy type of defects only and can give valuable information to complete the observations made by TEM. In this specific case, TEM was used to determine the type and size of defect clusters that are not accessible to the PAS technique. Indeed, the interstitial type of loops cannot trap the positrons at all and the microvoids observed specifically in Fe irradiated to high dose are perfect traps for positrons but are too large and too scarce to be quantitatively analyzed by PAS. Thus both techniques are to be considered as fully complementary to characterize the matrix damage.

Comparing PAS with APT and SANS techniques, at a first sight one could say that they are totally different as they are based on distinct physical basis. But, in the present case it appears that they do mainly detect the same defects, namely solute clusters with or without the presence of vacancies in the same site. By APT, solute atoms are detected, while no vacancies can be observed. This is in fact the opposite of what is detected by PAS. Therefore, the size seen by PAS is strongly underestimated. Nevertheless, also for the binary Fe–Cu alloys, where the PAS size has been given as vacancies and copper atoms, the obtained PAS size is smaller than the one of APT. This indicates that the clusters are diluted, as indicated by APT. This leads to an additional underestimation of the sizes by the PAS technique.

On the other hand, for all the materials, the number density of vacancy-type clusters detected by PAS is higher than the number density of solute clusters detected by APT (Fig. 4). The difference may come from the presence of vacancy clusters not associated with solute atoms. It can also reflect the contribution of very small vacancy–solute complexes not taken into account by APT. Indeed, the solute clusters detected by APT correspond to clusters containing more than about ten solute atoms in the real material (corresponding to five solute atoms in the reconstructed material, because of the detector efficiency of about 50%).

Furthermore, the formation of very small vacancy–solute complexes, not detected by APT, may also explain the differences observed in the FeMnNi alloy. Indeed, an important increase is observed in-between the two last irradiation doses in the PAS results, while for the APT results, saturation is observed. This could indicate that new defects were formed, which remain very small.

The SANS results also give information on about the same defects, but since the detection limit of this technique is about 0.5 nm, small defects will not be observed, leading to a higher average size of the observed defects and a lower average density. The comparison between the SANS data with those obtained from APT analysis make it clear that the information obtained from PAS needs to be integrated in order to reach a consensus on the apparent discrepancy observed between SANS and APT results. In fact, only the combination of the three techniques would allow a full qualitative description of the features induced by irradiation in the dilute alloys investigated here.

5. Conclusions

The results of a joint investigation using APT, SANS, TEM and PAS of neutron-irradiated pure Fe, ferritic model alloys and French 16MND5 RPV steel at 300 °C were presented. Starting point is a careful discussion of the effects of both composition and irradiation conditions on radiation damage obtained from each method individually. APT investigation is mainly devoted to the matrix composition and to composition, size and density of solute clusters; a decorated dislocation loop has also been identified. SANS analysis is sensitive to volumetric defects of both vacancy- and solute-type while providing robust spatial averages. TEM analysis is concentrated on the size distribution and type of dislocation loops; nanovoids have also been detected for pure Fe. PAS analysis is devoted to small vacancy-rich defects. Complementarities and overlaps of the applied techniques were identified.

The following conclusions can be drawn on the evolution of defect-solute clusters under neutron irradiation and on the effects of alloy composition and fluence within the covered range of conditions:

The neutron irradiation of various Fe-based alloys promoted the formation of nanometer-size features. They correspond to point defects and solute clusters.

The former can be interstitial in type (dislocation loops), or/and vacancy in type (cavities or voids). The addition of either Cu or, Mn and/or Ni is found to hinder their formation and suppress their growth (for both types). With dose, these features called generally matrix damage, appeared to grow. The most striking finding is that none of such defect has been observed in the complex RPV steel studied even after 0.2 dpa irradiation. The formation of solute clusters depends strongly on the chemical composition of the matrix and on the irradiation dose. In Cu-content alloys, Cu-rich precipitates were observed right after the lowest dose of irradiation. Their size appears to grow with dose but a close cross-comparison of the results obtained by different techniques allows to conclude that this type of solute clusters will be serving as a trap for the continuous vacancy flux. In fact, Cu atoms and vacancies like to co-cluster together. In the absence of Cu or in a very small amount, Mn and/or Ni rich nano-features have been observed but only after a high dose of irradiation (0.1 dpa in this investigation corresponding to 40 years of operation). Several indications have been found that demonstrate that these local enrichment is most probably due to an irradiation-induced segregation of Mn and/or Ni on the created interstitial loops. There is in fact a strong correlation between the so-called matrix damage and the solute elements present in the steels.

Finally, it is recognized that a careful and a rational cross-comparison between all techniques appear to be still needed to gain better quantitative information on the irradiation damage in RPV

steels. Furthermore, results reported in this paper concerned materials irradiated in a test reactor, at higher flux than RPV steels in industrial pressurized water reactor. It is therefore necessary to take account of the flux effect for the validation of models.

In a companion paper [54], the variation in yield stress during irradiation is explained in relation to the changes of the microstructure for the specific irradiation dose of 0.1 dpa. The different observed defects are taken as separate obstacles for the dislocation motion. At the end, their contributions are combined depending on their strength, to estimate the total irradiation-induced hardening.

Acknowledgements

The authors acknowledge the support of the PERFECT European Integrated Project under Contract No. FI6O-CT-2003-508840. The authors also thank S. Jumel and J.C. Van Duysen from EDF for providing the materials.

References

[1] T. Toyama, Y. Nagai, Z. Tang, M. Hasegawa, A. Almazouzi, E. van Walle, R. Gérard, Acta Mater. 55 (2007) 6852.
[2] P. Petrequin, A Review of Formulas for Predicting Irradiation Embrittlement of Reactor Vessel Materials, AMES Report No. 6, EUR 16455 EN, Office for Official Publications of the European Communities, Luxembourg, 1996.
[3] G.R. Odette, Scripta Metall. 17 (1983) 1183.
[4] S.B. Fisher, J.T. Buswell, Int. J. Press. Vessels Pip. 27 (1987) 91.
[5] G.R. Odette, B.D. Wirth, D.J. Bacon, N.M. Ghoniem, MRS Bull. (2001) 176.
[6] E. Vincent, C.S. Becquart, C. Domain, Nucl. Instrum. Methods B 255 (2007) 78.
[7] J.-P. Massoud, S. Bugat, J.-L. Boutard, D. Lidbury, S. Van Dyck, F. Sevini, PERFECT: Prediction of Irradiation Damage Effects on Reactor Components, in: G. Van Goethem, P. Manolatos, M. Hugon, V. Bhatnagar, S. Casalta, M. Deffrennes (Eds.), FISA 2006 – EU research and training in reactor systems, European Commission, Directorate-General for Research, Euratom, 2006 p. 107.
[8] P. Auger, P. Pareige, S. Welzel, J.-C. Van Duysen, J. Nucl. Mater. 280 (2000) 331.
[9] R.G. Carter, N. Soneda, K. Dohi, J.M. Hyde, C.A. English, W.L. Server, J. Nucl. Mater. 298 (2001) 211.
[10] S.C. Glade, B.D. Wirth, G.R. Odette, P. Asoka-Kumar, P.A. Sterne, R.H. Howell, Philos. Mag. 85 (2005) 629.
[11] J. Kocik, E. Keilova, J. Cizek, I. Prochazka, J. Nucl. Mater. 303 (2002) 52.
[12] M.K. Miller, B.D. Wirth, G.R. Odette, Mater. Sci. Eng. A 353 (2003) 133.
[13] Y. Nagai, Z. Tang, M. Hasegawa, T. Kanai, M. Saneyasu, Phys. Rev. B 63 (2001) 134110.
[14] M. Lambrecht, L. Malerba, A. Almazouzi, J. Nucl. Mater. 378 (2008) 282.
[15] E. Meslin, B. Radiguet, P. Pareige, A. Barbu, J. Nucl. Mater. 399 (2010) 137.
[16] F. Bergner, M. Lambrecht, A. Ulbricht, A. Almazouzi, J. Nucl. Mater. 399 (2010) 129.
[17] M. Hernández-Mayoral, D. Gómez-Briceño, J. Nucl. Mater. 399 (2010) 146.
[18] M. Lambrecht, A. Almazouzi, J. Nucl. Mater. 385 (2009) 334.
[19] M.K. Miller, Atom Probe Tomography, Plenum Publishers/Kluwer Academic, 2000.
[20] J. Kohlbrecher, W. Wagner, J. Appl. Crystallogr. 33 (2000) 804.
[21] M.H. Mathon, A. Barbu, F. Dunstetter, F. Maury, N. Lorenzelli, C.H. de Novion, J. Nucl. Mater. 245 (1997) 224.
[22] O. Glatter, J. Appl. Crystallogr. 13 (1980) 7.
[23] M.L. Jenkins, M.A. Kirk, Characterization of Radiation Damage by Transmission Electron Microscopy, Institute of Physics, Bristol, 2001.
[24] J.W. Edington, Practical Electron Microscopy in Materials Science, Ed. Macmillan Philips Technical Library, 1965.
[25] M. Eldrup, B.N. Singh, J. Nucl. Mater. 251 (1997) 132.
[26] M.J. Puska, R.M. Nieminen, Rev. Mod. Phys. 66 (1994) 841.
[27] M. Jardin, M. Lambrecht, A.A. Rempel, Y. Nagai, E. van Walle, A. Almazouzi, Nucl. Instrum. Methods A 568 (2006) 716.
[28] A. Vehanen, P. Hautojärvi, J. Johansson, J. Yli-Kauppila, Phys. Rev. B 25 (1982) 762.
[29] M. Lambrecht, A. Almazouzi, J. Phys. Conf. Ser., accepted for publication..
[30] P. Pareige, B. Radiguet, A. Barbu, J. Nucl. Mater. 352 (2006) 75.
[31] K. Fujii, K. Fukuya, N. Nakata, K. Hono, Y. Nagai, M. Hasegawa, J. Nucl. Mater. 340 (2005) 247.
[32] K. Fukuya, K. Ohno, H. Nakata, S. Dumbill, J.M. Hyde, J. Nucl. Mater. 312 (2003) 163.
[33] B. Radiguet, A. Barbu, P. Pareige, J. Nucl. Mater. 360 (2007) 104.
[34] B. Radiguet, P. Pareige, A. Barbu, Nucl. Instrum. Methods B 267 (2009) 1496.
[35] M.K. Miller, M.A. Sokolov, R.K. Nanstad, K.F. Russell, J. Nucl. Mater. 351 (2006) 187.
[36] M.K. Miller, K.F. Russell, J. Nucl. Mater. 371 (2007) 145.
[37] M.K. Miller, R.K. Nanstad, M.A. Sokolov, K.F. Russell, J. Nucl. Mater. 351 (2006) 216.
[38] M.K. Miller, Atom Probe Tomography: Analysis at the Atomic Level, Kluwer Academic/Plenum, New York, NY, 2000.
[39] The precipitated volume fraction was calculated with the proportion of solute atoms. It is more precise than the value calculated with the mean radius and the number density of clusters because some clusters were located at the edge of the analysis cylinder and the statistical error on the mean radius is not negligible.
[40] E. Meslin, A. Barbu, L. Boulanger, B. Radiguet, P. Pareige, K. Arakawa, C.C. Fu, J. Nucl. Mater. 382 (2008) 190–196.
[41] E. Meslin, A. Barbu, P. Pareige, B. Radiguet, submitted for publication..
[42] G. Solt, F. Frisius, W.B. Waeber, P. Tipping, Irradiation induced precipitation in model alloys with systematic variation of Cu, Ni and P content: a small angle neutron scattering study, in: A.S. Kumar, D.S. Gelles, R.K. Nanstadt, E.A. Little (Eds.), Effects of Radiation on Materials: 16th International Symposium, ASTM STP 1175, ASTM, Philadelphia, 1993, p. 444.
[43] A.C. Nicol, M.L. Jenkins, M.A. Kirk, Mater. Res. Soc. Symp. Proc. 50, paper R1.3, 2000.
[44] F. Ebrahimi, D.T. Hoelzer, D. Venables, V. Krishnamoorthy, Development of a Mechanistic Understanding of Radiation Embrittlement in Reactor Pressure Vessel Steels, Final Report NUREG/CR-5063 MEA-2268, 1988.
[45] M. Eldrup, B.N. Singh, S.J. Zinkle, T.S. Byun, K. Farrell, J. Nucl. Mater. 307–311 (2002) 912.
[46] K. Verheyen, M. Jardin, A. Almazouzi, J. Nucl. Mater. 351 (2006) 209.
[47] A. Seeger, M. Rühle, Ann. Phys. 11 (1963) 216.
[48] F. Bergner, A. Ulbricht, M. Hernandez-Mayoral, P.K. Pranzas, J. Nucl. Mater. 374 (2008) 334.
[49] P.M. Derlet, S.L. Dudarev, Prog. Mater. Sci. 52 (2007) 299.
[50] B. Radiguet, Etude de la formation d'amas diffus de solutés sous irradiation dans des alliages modèles ferritiques, Ph.D. thesis, University of Rouen, 2004.
[51] F. Vurpillot, A. Bostel, D. Blavette, Appl. Phys. Lett. 76 (2000) 21.
[52] A. Ulbricht, F. Bergner, J. Böhmert, M. Valo, M.-H. Mathon, A. Heinemann, Philos. Mag. 87 (2007) 1855.
[53] K. Sumiyama, T. Yoshitake, Y. Nakamura, J. Phys. Soc. Jpn. 53 (1984) 3160.
[54] M. Lambrecht, L. Malerba, A. Almazouzi, M. Hernández-Mayoral, D. Gómez-Briceño, E. Meslin, B. Radiguet, P. Pareige, F. Bergner, J. Nucl. Mater. 406 (2010) 84–89.
[55] S. Raoul, B. Marini, A. Pineau, J. Nucl. Mater. 257 (1998) 199.
[56] M. Karlik, I. Nebdal, J. Siegel, Mater. Sci. Eng. A 357 (2003) 423.
[57] M. Isacsson, T. Narström, Mater. Sci. Eng. A 271 (1999) 224.